Optics Letters

Focusing light in biological tissue through a multimode optical fiber: refractive index matching

Raphaël Turcotte,[1,2] Carla C. Schmidt,[2] Nigel J. Emptage,[2] and Martin J. Booth[1,*]

[1]Department of Engineering Science, University of Oxford, Parks Road, Oxford OX1 3PJ, UK
[2]Department of Pharmacology, University of Oxford, Mansfield Road, Oxford OX1 3QT, UK
*Corresponding author: martin.booth@eng.ox.ac.uk

Received 13 March 2019; revised 28 March 2019; accepted 30 March 2019; posted 1 April 2019 (Doc. ID 361164); published 2 May 2019

Controlling light propagation through a step-index multimode optical fiber (MMF) has several important applications, including biological imaging. However, little consideration has been given to the coupling of fiber and tissue optics. In this Letter, we characterized the effects of tissue-induced light distortions, in particular those arising from a mismatch in the refractive index of the pre-imaging calibration and biological media. By performing the calibration in a medium matching the refractive index of the brain, optimal focusing ability was achieved, as well as a gain in focus uniformity within the field-of-view. These changes in illumination resulted in a 30% improvement in spatial resolution and intensity in fluorescence images of beads and live brain tissue. Beyond refractive index matching, our results demonstrate that sample-induced aberrations can severely deteriorate images from MMF-based systems.

https://doi.org/10.1364/OL.44.002386

Focusing laser light some distance away from the distal end of a step-index multimode optical fiber (MMF) (away from the source) is of particular interest in biological sensing and imaging applications where the small diameter (<0.2 mm) of the MMF minimizes invasiveness and enables the multiplexing of measurements [1–3]. As light propagates in an MMF, unpredictable phase delays and coupling occur between modes, causing the output intensity profile from a Gaussian input to have a speckle-like appearance. Several methods have been developed to evaluate this deterministic transformation such that the complex light field propagating through MMF could be controlled using active wavefront shaping [4–6]. In each case, a calibration procedure involving distal optical components is necessary; however, the impact of distal optical aberrations present during calibration versus imaging is not known. In this Letter, we characterize the effects of a refractive index mismatch between the biological and calibration media on focus formation in the context of brain imaging using one-photon fluorescence point-scanning microscopy through MMF. This type of mismatch is commonly encountered as calibrations are routinely performed in air, while imaging is performed in brain tissue [1–3].

The system comprised three units [1,7]: a source, a wavefront shaping, and a calibration unit (Fig. 1). In the source unit, laser light (CrystaLaser, DL488-020-S, CW, 488 nm) was coupled into two single-mode optical fibers (Thorlabs, P1-488PM-FC-2 and P1-405B-FC-5) for delivery to the wavefront shaping and calibration unit, respectively. The wavefront shaping unit was composed of a liquid-crystal spatial light modulator (LC-SLM, Meadowlark Optics, HSPDM512), the MMF [Thorlabs, FG050UGA, core diameter 50 μm,

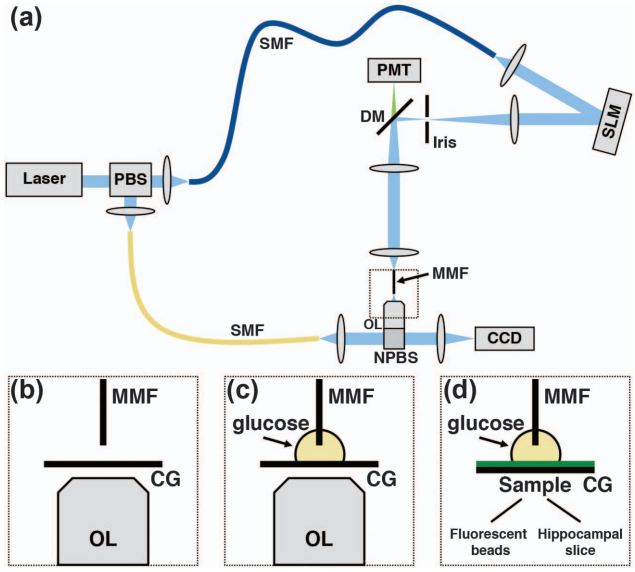

Fig. 1. (a) Simplified schematic of the optical system (SMF, single mode optical fiber; PBS, polarizing beam splitter; PMT, photomultiplier tube; DM, dichroic mirror; SLM, spatial-light modulator; NPBS, non-polarizing beam splitter; MMF, CCD, charge-coupled device; multimode fiber; and OL, objective lens). (b–d) Schematics of the experimental setup: (b) for air calibration, (c) for glucose (refractive index matching) calibration, and (d) for imaging (CG, coverglass).

numerical aperture (NA) 0.22], and relay optics. The LC-SLM was conjugated to an iris, letting through the on-axis first-order diffraction beam for wavefront shaping [8]. The modulated wavefront was then given a circular polarization with a quarter-wave plate (Thorlabs, WPQ05M-488) before it reached the MMF because this polarization state is power-invariant in an MMF [9]. Finally, the calibration unit imaged the MMF output at the distal facet with a microscope objective lens (Olympus, Plan N 20×, NA 0.4) and an achromatic doublet lens ($f = 150$ mm) on a CCD camera (Basler pilot, piA640-210gm), where it interfered with the reference beam. A second quarter-wave plate was positioned behind the objective to make the polarization linear and parallel to that of the reference beam. The calibration camera was also used to capture the illumination focal volume, but without the reference beam being present.

All fiber segments were cut to a length of 2.0 cm and glued into a ferrule (Thorlabs, CF128-10) before being positioned into the optical system. Subsequently, the wavefront shaping module was aligned with the calibration unit by imaging the distal facet of the MMF on the calibration camera. Then, the coupling of light into the MMF was optimized by translating axially and laterally the lens located immediate before (Thorlabs, C240TME-A, NA 0.5). To focus a known distance away from the MMF distal facet, the wavefront-shaping unit was moved by such a distance from the calibration unit before performing the calibration (to select an axial focusing plane by imaging it onto the camera). Data were acquired 50 μm away from the distal facet, unless otherwise mentioned. The calibration consisted of the acquisition of the transmission matrix (TM), which describes the field transformation between two planes within the optical system [1]. The TM enabled the determination of the linear superposition of input modes (2401 modes) across the proximal fiber facet, or equivalently the LC-SLM pattern generating the shaped wavefront, required to produce a single focus at a specific location of the distal fiber facet. The fiber could support 2504 modes.

First, we assessed the effect of a refractive index mismatch between the calibration and imaging media on the illumination focus. For a single measurement, the illumination focus was captured with four different illumination powers (optical densities from 0 to 3) to reconstruct high dynamic range images [3]. Three metrics were used to characterize focus quality: the peak intensity, the intensity enhancement factor (IEF), and the lateral full width at half-maximum (FWHM). The IEF was defined as the peak intensity divided by the average intensity from all pixels within the central 50 μm diameter of the field imaged by the fiber. The FWHM was quantified by fitting a Gaussian profile to a line profile drawn through the focus.

The TM is frequently evaluated with the distal facet in air (with an air objective lens corrected for some thickness of glass). For several applications, fibers might be inserted in other milieus than air, such as an aqueous solution or biological tissue. The primary optical property affecting focusing that will differ in such cases is the index of refraction ($n_{air} = 1.00$, $n_{water} = 1.33$, and $n_{brain} = 1.37$ [10]). To quantify the effect of an index of refraction mismatch on focusing, we evaluated the FWHM and IEF of the illumination focal volume when the distal end of MMF were submerged in a solution of 22% glucose to mimic the rodent brain ($n_{glu,22\%} = 1.37$ [11]). A coverglass was located just below the desired focal plane. Calibrations were acquired with a media present between the MMF distal facet and the coverglass, either air or a 22% glucose solution, which will be referred to as the air and glucose calibration for the remainder of this Letter.

At the center of the imaged field, the peak intensity and IEF were 20 ± 11% and 11 ± 10% larger, respectively, when using the calibration acquired in a 22% glucose solution over the one acquired in air [$n = 6$, one-sided paired Wilcoxon signed rank (opWSR) test, $p_{value} = 0.016$] [Fig. 2(a)]. Similarly, the FWHM decreased from 1.28 ± 0.05 μm with the air calibration to 1.24 ± 0.05 μm with the 22% glucose one [$n = 6$, opWSR rank test, $p_{value} = 0.03$, Fig. 2(b)]. These results indicate that matching the refractive index of the calibration and imaging media will improve the signal-to-background ratio and the lateral width of the illumination focus. By analyzing the variation in peak intensity and FWHM as a function of the distance from the center of the fiber, we also observed that the peak intensity and FWHM were constant over a larger radius in the index-matched condition, thus providing a more uniform field-of-view [Figs. 2(c) and 2(d)]. Of note, we also compared focus quality achieved with calibrations acquired in air using an air objective lens corrected for 170 μm of glass with and without a coverglass in place. The illumination focal volume was then evaluated in air immediately at the fiber output in its center. The IEF indicates that better focusing was achieved when a coverglass was used during the calibration (Table 1; four segments per group, five trials per segment, one-sided paired t-test, ΔIEF = 7%, $p_{value} = 0.019$). This result indicates that aberrations in the

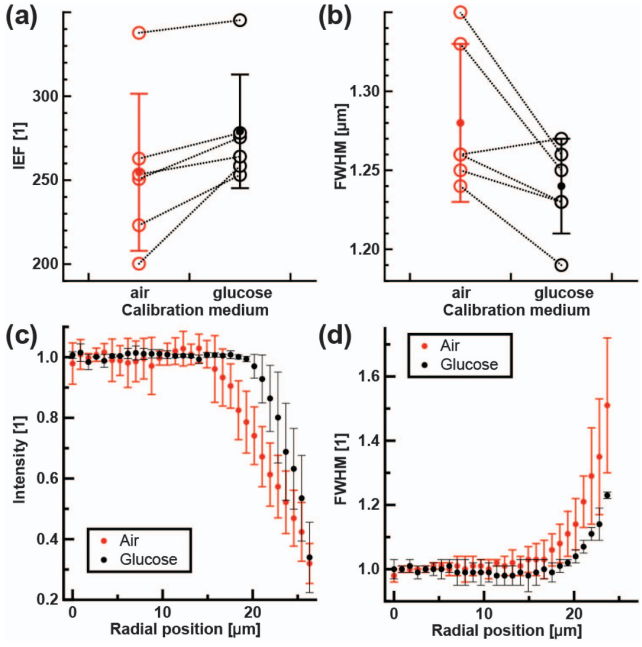

Fig. 2. Characterization of the illumination focal volume through an MMF in a 22% glucose solution. (a, b) Focal volume at the center of the MMF, characterized by (a) the IEF and (b) FWHM as a function of the calibration medium ($n = 6$ fiber segments, open circles represent individual measurements). (c, d) Radial variation in (c) peak intensity and (d) FWHM of the focal volume for a calibration done in air and in a 22% glucose solution ($n = 3$ fiber segments). Full circles are average values, and error bars represent the standard deviation.

Table 1. Effect of a Coverglass During Calibration in Air

Coverglass Thickness [μm]	FWHM [μm]	IEF [1]
0	1.30 ± 0.02	343 ± 7
170	1.30 ± 0.02	366 ± 5

calibration unit can also degrade the quality of the illumination focus.

Having demonstrated the improved illumination focus achieved when determining the TM in a medium having the same refractive index as the sample to be imaged, we characterized how calibrations performed in different media impacted the imaging of fluorescent beads. Beads [FluoSpheres carboxylate-modified microspheres, 1.0 μm, yellow-green fluorescent (505/515), 2% solids] were placed on a glass slide and immersed, together with the distal MMF facet, in a 22% glucose solution. Images were acquired with both an air [Fig. 3(a)] and a glucose calibration [Fig. 3(b)] at their respective optimal focal plane. Comparing the two conditions revealed that individual beads had a circular profile in images acquired with the glucose calibration (0.91 ± 0.05), whereas the bead shape was less symmetric for the air calibration (0.79 ± 0.11, circularity, $n = 36$, opWSR rank test, $p_{value} = 2.1 \times 10^{-6}$). Circularity was calculated after fitting an ellipse to individual beads and calculating the ratio of the minor to major axis. We also measured the FWHM of single beads and found that the ratio between the glucose and air calibration was 0.69 ± 0.17 ($n = 51$, Δ35%, opWSR test, $p_{value} = 3 \times 10^{-9}$). Most of the variability originated from the FWHM measured with the air calibration (2.1 ± 0.5 μm) [Fig. 3(c)], while the FWHM with the glucose calibration was more consistent between beads (1.37 ± 0.13 μm). This observation is in line with a more uniform illumination being achieved with the glucose calibration. However, the significant gain in peak intensity, a factor of 1.3 ± 0.2 ($n = 75$, opWSR test, $p_{value} = 1.0 \times 10^{-13}$) [Fig. 3(d)], was larger than that of the illumination peak intensity. This difference likely results from the detected fluorescence signal being a lateral and axial integration within the illumination focus. Thus, the latter result corresponds more closely to the actual improvement that will be achieved in images of biological samples [12].

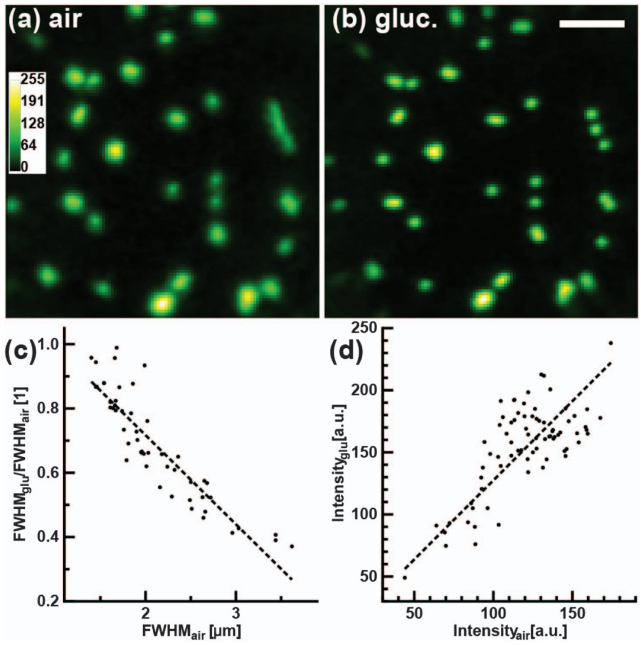

Fig. 3. Imaging of fluorescent beads through an MMF. (a, b) Images of 1.0-μm beads acquired with the TM determined from a calibration in (a) air and in (b) a 22% glucose solution. Scale bar: 10 μm. Images were normalized to the peak intensity in (b). (c) Graph of the FWHM ratio for individual beads from images acquired with the glucose TM over that of the air TM as a function of the FWHM measured from images acquired with the air TM ($n = 51$, slope = −0.3 μm^{-1}, $R^2 = 0.81$). (d) Graph of the peak intensity for individual beads from images acquired with the glucose calibration as a function of the peak intensity measured from images acquired with the air calibration ($n = 75$, slope = 1.3, $R^2 = 0.47$).

Deep-brain imaging is an important application for MMF-based microscopes because of the modest damage imparted to surrounding tissue as compared to alternative methods [1–3]. Representative images of a live neuron in organotypic hippocampal slices are shown in Figs. 4(a) and 4(b) (Wistar rats, thickness 350 μm). For visualization, CA1 pyramidal cells were patched with Alexa Fluor 488 fluorescent dye (0.5–1 mM, Life Technologies) for 3–5 min. To maintain slice health, imaging was performed in physiological Tyrode's solution (in mM: 120 NaCl, 2.5 KCl, 30 glucose, 2 CaCl2, 1 MgCl2, and 20 HEPES; Sigma Aldrich). Two calibrations were performed: in air and in Tyrode's solution. With the air calibration, no synaptic specializations (dendritic spines) were visible [Fig. 4(a)]. In contrast, dendritic spines were clearly visible with the Tyrode's calibration [Fig. 4(b)]. This improvement in spatial resolution and signal-to-background ratio was also apparent in the Fourier transform images [Figs. 4(c) and 4(d)], revealing

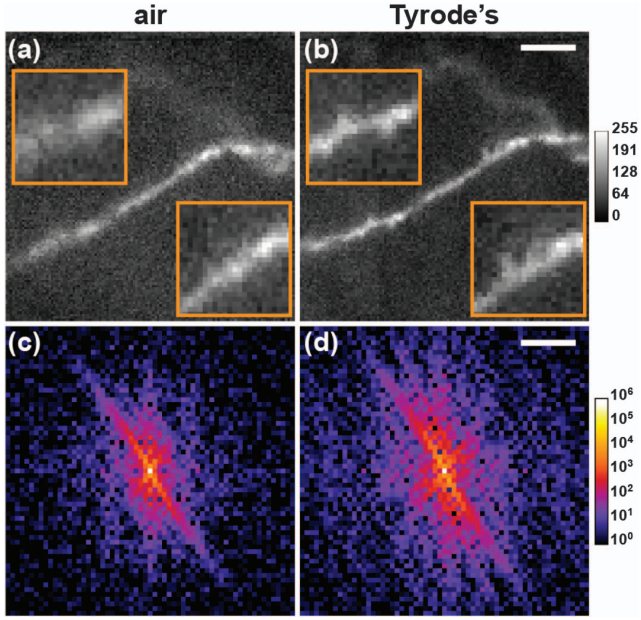

Fig. 4. Imaging of live neurons through an MMF in organotypic slices. (a, b) Images of a dendrite labelled with Alexa Fluor 488, acquired with the TM determined from a calibration in (a) air and in (b) a Tyrode's solution. Scale bar and inset width: 10 μm. Images were normalized to the peak intensity in (b). (c, d) Power frequency spectra of the images shown in (a, b), respectively. Scale bar: 0.22 μm^{-1}.

the larger spatial frequency bandwidth accessible with the Tyrode's calibration. In addition, the dendrite appeared tilted with respect to the focal plane with the air calibration. This observation has previously been assumed to reflect the actual position of the dendrite [1]; however, this is clearly erroneous as the dendrite lay within the focal plane of the Tyrode's image. In fact, it was the reduced uniformity in focusing ability with the air calibration that generated less resolved structures, appearing out-of-focus, at the circumference of the image.

A fiber-specific calibration is required to shape light through MMF for imaging. It is well known that such calibration will compensate not only distortions occurring inside the fiber, but proximal aberrations as well. We showed that this is not true for distal aberrations. Indeed, the ability to resolve subcellular, synaptic structure, essential when addressing many questions in neuroscience, is substantially improved when one takes account of the refractive index of brain tissue during the calibration. Even when focusing light at 488 nm through only 50 μm of tissue, a significant difference was measured, both in terms of focus quality and uniformity across the field-of-view.

The aberrations present when performing the calibration in air are akin to spherical aberrations. They nevertheless differ in that the light field at the distal facet, the interface where the refractive index changes, is not uniform and varies between fibers. Accordingly, the aberrated focal profile will be fiber dependent, depending on the spatial intensity and phase variations at the interface. It is also interesting to note that the lateral extent of the focus deteriorated when a mismatch was present, while spherical aberrations typically have a limited effect on this parameter [12]. We expect that as the NA is increased, so will the aberrations originating from a mismatch in the refractive index between the calibration medium and the sample. A fiber with a relatively low NA 0.22 was used in this study. Using fibers with higher NA is desirable because they would provide an increased spatial resolution, but also because high-NA MMF have been linked to a decreased sensitivity to bend translation [13,14]. In addition, two-photon fluorescence (2PF) MMF-systems are desirable because of the intrinsic optical sectioning they offer, and high-NA fibers would again be needed as 2PF efficiency increases nonlinearly with the NA [6,15].

Our results point to the importance of assessing the performance of MMF-based imaging systems, in the context of optical aberrations or in any other context, using the signal of interest. Indeed, the effects of refractive index matching on fluorescence imaging were substantial, while the improvements in illumination focus were moderate. This suggests that it might not be sufficient to look exclusively at the illumination, as is commonly done for MMF-based imaging systems, to characterize the impact on imaging performance. While we have emphasized the significance of these observations for biological imaging, our conclusion relating to the importance of considering distal aberrations applies to all applications requiring focusing light at the distal end of a MMF, including microfabrication [16], as well as other types of optical manipulation.

Funding. Biotechnology and Biological Sciences Research Council (BBSRC) (BB/P0273OX/1); H2020 European Research Council (ERC) (695140).

Acknowledgment. The authors thank Rudi Tong for technical assistance.

REFERENCES

1. S. A. Vasquez-Lopez, R. Turcotte, V. Koren, M. Plöschner, Z. Padamsey, M. J. Booth, T. Čižmár, and N. J. Emptage, Light: Sci. Appl. **7**, 110 (2018).
2. S. Turtaev, I. T. Leite, T. Altwegg-Boussac, J. M. P. Pakan, N. L. Rochefort, and T. Čižmár, Light: Sci. Appl. **7**, 92 (2018).
3. S. Ohayon, A. Caravaca-Aguirre, R. Piestun, and J. J. DiCarlo, Biomed. Opt. Express **9**, 1492 (2018).
4. R. Di Leonardo and S. Bianchi, Opt. Express **19**, 247 (2011).
5. T. Čižmár and K. Dholakia, Opt. Express **19**, 18871 (2011).
6. E. E. Morales-Delgado, D. Psaltis, and C. Moser, Opt. Express **23**, 32158 (2015).
7. M. Plöschner and T. Čižmár, Opt. Lett. **40**, 197 (2015).
8. M. A. Neil, M. J. Booth, and T. Wilson, Opt. Lett. **23**, 1849 (1998).
9. M. Plöschner, T. Tyc, and T. Čižmár, Nat. Photonics **9**, 529 (2015).
10. J. Binding, J. Ben Arous, J.-F. Leger, S. Gigan, C. Boccara, and L. Bourdieu, Opt. Express **19**, 4833 (2011).
11. D. R. Lide, *CRC Handbook of Chemistry and Physics*, 82nd ed. (Taylor & Francis, 2001).
12. R. Turcotte, Y. Liang, and N. Ji, Biomed. Opt. Express **8**, 3891 (2017).
13. D. Loterie, D. Psaltis, and C. Moser, Opt. Express **25**, 6263 (2017).
14. S. Bianchi, V. P. Rajamanickam, L. Ferrara, E. Di Fabrizio, C. Liberale, and R. Di Leonardo, Opt. Lett. **38**, 4935 (2013).
15. E. E. Morales-Delgado, S. Farahi, I. N. Papadopoulos, D. Psaltis, and C. Moser, Opt. Express **23**, 9109 (2015).
16. E. E. Morales-Delgado, L. Urio, D. B. Conkey, N. Stasio, D. Psaltis, and C. Moser, Opt. Express **25**, 7031 (2017).